Optics Letters

Plasmonic micropipe spectral filters in mid-infrared

Jian Xu,[1,†] Ang Wang,[2,†] and Yaping Dan[1,2,*]

[1]Center of Advanced Electronic Materials and Devices, Shanghai Jiao Tong University, Shanghai 200240, China
[2]University of Michigan and Shanghai Jiao Tong University Joint Institute, Shanghai Jiao Tong University, Shanghai 200240, China
*Corresponding author: yaping.dan@sjtu.edu.cn

Received 31 May 2019; revised 2 August 2019; accepted 17 August 2019; posted 20 August 2019 (Doc. ID 368926); published 6 September 2019

Multispectral analyzers based on nanostructured plasmonic spectral filters can potentially find a wide range of applications. However, spectral filters based on the widely reported microhole or ring arrays suffer from relatively wide filtering bands, resulting in a relatively low spectral resolution. In this work, we fabricate high-performance spectral filters based on vertically standing micropipes on a silver film. An infrared spectral microscope is used to investigate the properties of these micropipe spectral filters. The results indicate that the micropipe spectral filters have a full width at half-maximum ∼5 times smaller than the microhole filters at the same wavelength. Micropipe spectral filters are expected to significantly improve the spectral resolution of multispectral analyzers.

https://doi.org/10.1364/OL.44.004479

Two-channel spectral analyzers have been commercialized for monitoring indoor air quality by using two Fabry–Perot band-pass filters to catch the infrared absorption features of formaldehyde and carbon monoxide at two wavelengths [1–3]. A multispectral analyzer using multiple band-pass filters will expand its capability to detect more chemicals for a wider range of applications. However, the existing band-pass filters are based on the interference of lights passing through multiple layers of films with periodically modulated refractive index [4]. The tuning of the band-pass wavelengths relies on the adjustment of film thicknesses [5]. Each band-pass wavelength requires a series of fabrication processes, including photolithography, reactive ion etching, and deposition of films. In practice, it is extremely challenging to fabricate a multispectral analyzer by adopting this approach. In recent years, novel approaches to achieve spectral selectivity based on plasmonic antennas [6,7], deep-subwavelength resonant apertures [8,9], and silicon nanowires [10] have been proposed. As an alternative approach, it was found that nanostructured plasmonics can be used to construct band-pass filters [11–14]. The structures of these filters are as simple as an array of periodically ranged subwavelength holes or rings in a gold or silver film. The central wavelength of the band-pass filters is determined by the periodicity of the subwavelength structures, instead of the film thickness. This interesting feature allows us to fabricate millions of band-pass filters across the spectrum from visible to far infrared in one cycle of microfabrication. However, the full width at half-maximum (FWHM) of these band-pass spectral filters is relatively large, approximately 20% of the band-pass central wavelength [15]. Multispectral analyzers made of these spectral filters have poor spectral resolution and difficulty catching the spectral features of absorption. Although reconstruction algorithms can be used to improve the spectral resolution by exploiting the spectral redundancy of closely spaced filters in the spectrum [16], it is still crucial to construct plasmonic spectral filters with a narrow FWHM.

In this work, we find that narrow band-pass filters can be constructed by using subwavelength micropipes that are vertically standing on a silver film and arranged in a periodic order. The micropipes are fabricated in a liftoff process to simplify the fabrication procedure. The fabricated micropipe arrays have a spectral FWHM of ∼4% central wavelength, ∼5 times smaller than that of the standard microhole arrays. It is expected that multispectral analyzers made of these micropipe spectral filters will have a much higher spectral resolution.

We previously showed that a miniaturized spectral analyzer in mid-infrared (MIR) can be constructed by using plasmonic microhole arrays in gold (Au) thin film as multispectral filters [15]. The band-pass transmission spectrum of the filters can be shifted in MIR (3–13 μm) by simply tuning the periodicity of the hole arrays. However, the transmission spectrum of the microhole filters has a relatively large FWHM that is typically around 20% of the central wavelength. The miniaturized spectral analyzer built on these plasmonic multispectral filters suffers from a spectral resolution much poorer than the Fourier transform infrared (FTIR) spectroscopy. Consequently, the potential of the plasmonic spectral analyzer to find applications is compromised. Interestingly, Degiron *et al.* [17] reported that the transmission spectrum of metallic microhole filters will narrow down by increasing the hole depth due to the fact that the surface-plasmons (SPs) on the top and bottom surfaces are decoupled for deeper holes. However, it is challenging to use physical vapor deposition (PVD) systems to deposit a film with thickness close to micrometer scale. Fortunately, we found in the simulations and experiments that a periodical micropipe structure on the metallic film will also decouple the SPs on

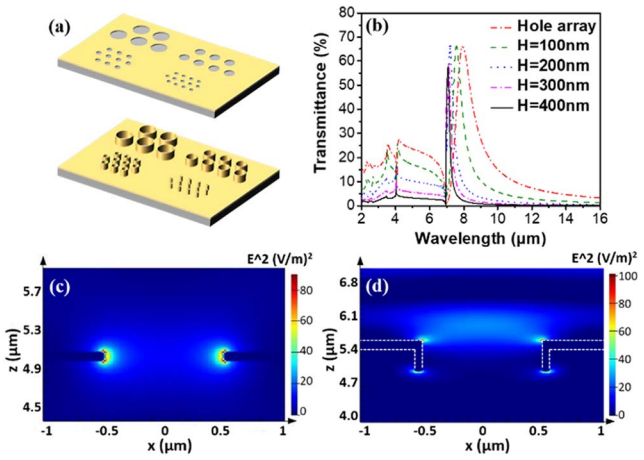

Fig. 1. (a) Schematic of microholes and micropipes based multispectral filters. (b) Simulated transmission spectra of microhole array and micropipe arrays with different heights, where the period and diameter are fixed at 2 μm and 1 μm, respectively. Simulated E-field distribution inside the (c) holes and (d) pipes.

the two surfaces, similar to the microhole arrays in a thick film. Finite difference time domain (FDTD) simulations were performed using Lumerical FDTD solution with a time step of 0.05109 fs and an auto non-uniform mesh accuracy of 2. Periodic boundary conditions were applied at the x and y boundaries and perfectly matched layers (PMLs) at the z boundaries. The simulation results show that as we increase the height of the micropipes on a 100 nm thick silver film from 0 nm (corresponding to holes) to 400 nm [Fig. 1(a)], the FWHM of the zero-order peak narrows from ∼1.5 μm down to ∼300 nm [Fig. 1(b)]. When the height is larger than 400 nm, the amplitude of the transmission peak starts to drop, which is not desirable. Figures 1(c) and 1(d) show their simulated E-field distribution of the periodic microhole and micropipe structures, respectively. It shows clearly that the SPs on the top and bottom surfaces of the microholes are physically coupled, while for micropipes, the SPs on the two surfaces are decoupled.

To fabricate the micropipe array structure, we adopted an optimized lift-off process with deep undercuts by utilizing a copolymer electron beam resist (methyl methacrylate and methacrylic acid, AR-P 617, AllResist GmbH). See the Experimental section for details. Briefly, we spin-coated and pre-baked twice the copolymer on a Ge wafer, forming a total thickness of 600 nm. A 180 nm thick layer of CSAR62 resist was then spin-coated on the top of the 600 nm thick copolymer resist. Electron beam lithography was carried out in the e-beam system (RAITH EBPG5200 HS) operating at the accelerated voltage of 100 keV. The beam current was set at 1 nA with the spot size of ∼4 nm. The doses were chosen at 210 μC/cm^2 according to our experimental test. The exposed samples were developed in a pure methyl isobutyl ketone (MIBK) solution at room temperature for 40 s. A layer of 150 nm thick silver metal was deposited in the Denton sputtering machine under the sputtering power of 50 W with an Ar gas flow rate of 25 sccm and chamber pressure of 5.2 mTorr. The silver target was fixed at an angle of 45° respective to the rotating sample surface so that the metal film could be uniformly deposited at the sidewall

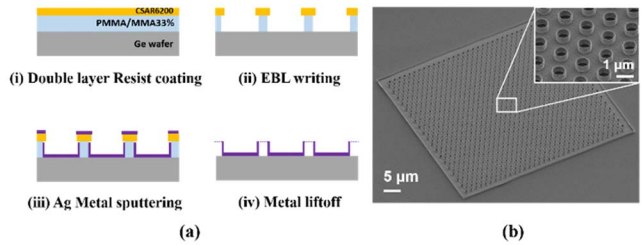

Fig. 2. (a) Fabrication process flow of the micropipe array. (b) SEM tilt view of the micropipe array.

of the resist cylinder array and the substrate surface. The metal-coated sample was then immersed in the acetone solvent for about 5 min to lift off the unwanted metal at un-exposed areas. The process flow is illustrated in Fig. 2(a), and the scanning electron microscopic (SEM) image of the fabricated periodic micropipe structure is shown in Fig. 2(b). The periodic micropipe structure was then covered with a layer of Ge before the FTIR measurements.

We measured the transmission spectra of fabricated micropipe arrays with a microscopic FTIR spectroscope. The light source launched from the backside of the sample and the detector was placed on the front side. The height of the micropipes was ∼400 nm. The ratio of the micropipe inner-diameter versus the period of the micropipe was fixed at 1:2. As the period increased from 1.5 μm to 3 μm, the spectral peak shifted from ∼5 μm to ∼11 μm, as shown in Fig. 3(a). The transmittance of each array was measured separately, which means that the measured results were localized transmittance that equals to the ratio of transmitted light intensity through one array to the incident light intensity only on this array. We also performed FDTD simulations for these micropipes as shown in Fig. 3(b). The simulation results are largely consistent with the experimental results except that the transmission peaks in the measured spectra are clearly smaller as the period of the micropipe array reduces. This is because the proximity effect of electron beam exposure becomes stronger for smaller sizes, resulting in an inner diameter smaller than designed. A smaller ratio of diameter to period will reduce the transmission amplitude. For comparison, we also fabricated an array of microholes in silver film with the same thickness on Ge substrate. The hole diameter versus the hole period was set at 1:2. We found that FWHMs of the micropipe transmission peaks were all reduced ∼5 times in comparison with the microholes with the same period [Figs. 3(c) and 3(d)]. The high-order harmonic transmission peaks visible in the microhole arrays were also largely suppressed in the micropipe arrays. It shows that micropipe arrays are potentially better alternatives as plasmonic multispectral filters for a miniaturized spectral analyzer.

To visualize the wavelength selectivity of the new micropipe array filters, we imaged the spatial transmittance distribution of the four arrays at the specific wavelengths of their peak positions: 5.29 μm, 7.01 μm, 8.80 μm, and 10.69 μm, respectively. The micropipe arrays were all fabricated on the same chip, and each array had an area of around 50 × 50 μm^2. The transmittance window 15 × 15 μm^2 was used to scan over the whole chip at a step of 2 μm. The transmittance at each wavelength was coded in a colorful image, as shown in Fig. 4. At each resonance wavelength, the transmittances of the other arrays are

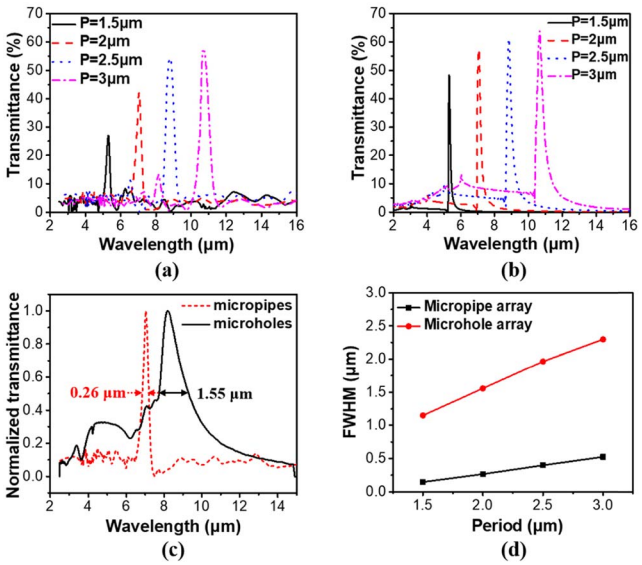

Fig. 3. (a) Experimentally measured spectra of 400 nm high micropipe arrays with period from 1.5 μm to 3 μm where the ratio of diameter to period is 1:2. (b) Corresponding simulated results of micropipe arrays. The decline in transmittance for smaller periods can be explained by the cylindrical waveguide theory [17]. (c) Measured transmission spectra and their FWHMs of periodic micropipe and microhole arrays where their period and diameter are both 2 μm and 1 μm, respectively. (d) FWHMs of experimentally measured transmission peaks of microhole and micropipe arrays with periods from 1.5 μm to 3 μm, respectively.

extremely low, which is consistent with the measured transmission spectra in Fig. 3(a). All the measurements illustrate the fabricated four MIR filters based on micropipe arrays can filter light efficiently with quite low crosstalk between each other.

In this work, we demonstrated a simple liftoff process to fabricate vertically standing micropipes. The periodically spaced micropipes on the silver film are narrow band-pass spectral filters due to surface plasmonic resonances. The FWHM of these filters is ∼5 times smaller than that of the microhole arrays at the same wavelength due to the decoupling of the plasmonic resonance at the top and bottom surfaces. As a result, multispectral analyzers based on micropipe filters are expected to have a much higher spectral resolution.

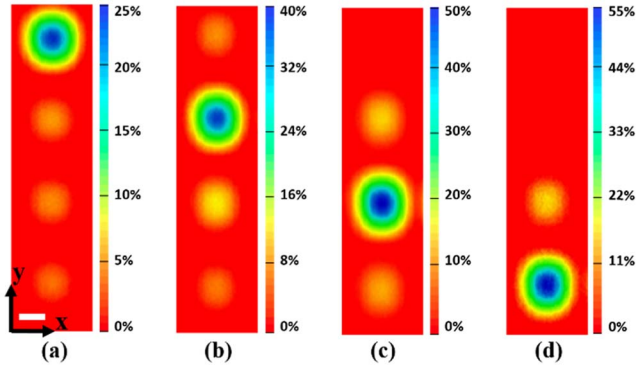

Fig. 4. Mid-infrared transmission 2D maps of the micropipe array filters are plotted at four different wavelengths: (a) 5.29 μm, (b) 7.01 μm, (c) 8.80 μm, and (d) 10.69 μm. Scale bar: 30 μm.

Experimental. We used a liftoff process to fabricate the vertically standing micropipes, which requires deep undercuts in the resists. Poly-methyl methacrylate (PMMA) is an electron-beam-sensitive resist that has higher sensitivity for lower molecular weight [18,19]. The widely used strategy to create undercuts for liftoff is to use two layers of PMMA with the top and bottom layers having a large and small molecular weight, respectively [20,21]. However, the sensitivity tunability of PMMA is relatively small, and it is therefore difficult to create deep undercuts [22].

In this work, we create deep undercuts in a bilayer-resist structure consisting of CSAR62 on top of a copolymer [methyl methacrylate (MMA) and methacrylic acid, AR-P 617, AllResist GmbH] [23–25] by exploiting the highly tunable sensitivity of the copolymer to electron beam exposure. In comparison with the polymer composed of MMA alone, the copolymer has methacrylic acids randomly distributed in the polymerization chain. Every two methacrylic acids, if adjacent to each other in the polymer chain, will form a 6-ring via dehydration by thermal treatment at elevated temperature. The 6-ring is much easier to break by electron beam exposure compared to the aliphatic chain in PMMA. After electron beam exposure, the copolymer will break into pieces of small molecules that can be dissolved in developers. We systematically measured the development rates of the copolymer and the CSAR62 resists developed in pure MIBK solution for 40 s. As the baking temperature increases from 220°C to 260°C, the concentration of 6-rings becomes higher; as a result, the development rate of the copolymer is increased by 2 to 4 times for the different exposure doses. In contrast, the CSAR62 possesses a relatively stable development rate. This contrast in development rate allows us to create a deep undercut in the bilayer resist with CSAR62 on top of the copolymer composed of MMA and methacrylic acid.

The deep undercut facilitates the success of the liftoff process. The profile of the undercut determines the final three-dimensional film structure. To examine how the dosage affects the undercut profile, we spin-coated a bilayer resist consisting of 200 nm thick CSAR62 resist on top of 600 nm thick copolymer. An array of bilayer resist cylinders was created by e-beam exposure with the doses ranging from 180 $\mu C/cm^2$ to 230 $\mu C/cm^2$. Since the CSAR62 and copolymer are positive resists, we exposed the area outside the cylinders that are about 600 nm in diameter. The proximity effect may cause a non-uniform energy deposition. To correct this non-uniformity, Monte Carlo simulations were performed to ensure uniform energy deposition. The e-beam exposed patterns were then developed in MIBK for 40 s and 50 s, respectively. The cross section of each resist cylinder was examined with SEM. The undercut size is defined as the difference in radius of the top CSAR62 and the neck of the bottom layer. The angle is the one between the side wall and the substrate surface. As the dosage ramps up, both the undercut size and the angle linearly increase. At the dose of 220 $\mu C/cm^2$, the angle crosses 90°. At the dose of 230 $\mu C/cm^2$, the undercut is more than 230 nm and the radius of the bottom layer cylinder is less than 140 nm, which is too thin to remain standing up against the surface tension of the MIBK developer. The development time has little impact on the undercut size and the angle. The formation of large undercuts and vertical resist pillars gives us a lot

of flexibility in how to deposit materials and what material structures to create.

Funding. National Natural Science Foundation of China (61874072); Science and Technology Commission of Shanghai Municipality (16JC1400405).

Acknowledgment. The microfabrication was carried out at the center of Advanced Electronic Materials and Devices (AEMD), and the infrared spectral microscopy was performed at the Instrumental Analysis Center (IAC), Shanghai Jiao Tong University.

†These authors contributed equally to this Letter.

REFERENCES

1. G. E. Ewing, W. E. Thompson, and G. C. Pimentel, J. Chem. Phys. **32**, 927 (1960).
2. L. Jun, T. Qiulin, Z. Wendong, X. Chenyang, G. Tao, and X. Jijun, Measurement **44**, 823 (2011).
3. T.-V. Dinh, I.-Y. Choi, Y.-S. Son, and J.-C. Kim, Sens. Actuators B Chem. **231**, 529 (2016).
4. S. Kinoshita and S. Yoshioka, ChemPhysChem **6**, 1442 (2005).
5. G. Kedawat, P. Kumar, Y. Vijay, and B. K. Gupta, J. Mater. Chem. C **3**, 6745 (2015).
6. S. Zhang, Z. Ye, Y. Wang, Y. Park, G. Bartal, M. Mrejen, X. Yin, and X. Zhang, Phys. Rev. Lett. **109**, 193902 (2012).
7. J. Le Perchec, Y. Desieres, N. Rochat, and R. Espiau de Lamaestre, Appl. Phys. Lett. **100**, 113305 (2012).
8. Y. Büyükalp, P. B. Catrysse, W. Shin, and S. Fan, Appl. Phys. Lett. **105**, 011114 (2014).
9. Y. Buyukalp, P. B. Catrysse, W. Shin, and S. Fan, ACS Photon. **4**, 525 (2017).
10. H. Park, Y. Dan, K. Seo, Y. J. Yu, P. K. Duane, M. Wober, and K. B. Crozier, Nano Lett. **14**, 1804 (2014).
11. T. W. Ebbesen, H. J. Lezec, H. Ghaemi, T. Thio, and P. Wolff, Nature **391**, 667 (1998).
12. A. G. Brolo, R. Gordon, B. Leathem, and K. L. Kavanagh, Langmuir **20**, 4813 (2004).
13. C. Genet and T. Ebbesen, Nature **445**, 39 (2007).
14. Q. Chen, D. Chitnis, K. Walls, T. D. Drysdale, S. Collins, and D. R. Cumming, IEEE Photon. Technol. Lett. **24**, 197 (2012).
15. A. Wang and Y. Dan, Sci. Rep. **8**, 11257 (2018).
16. B. Craig, J. Meng, V. R. Shrestha, J. J. Cadusch, and K. B. Crozier, in *Conference on Lasers and Electro-Optics* (Optical Society of America, 2019), paper JTu2A.48.
17. A. Degiron, H. Lezec, W. Barnes, and T. Ebbesen, Appl. Phys. Lett. **81**, 4327 (2002).
18. Y. Chen, Microelectron. Eng. **135**, 57 (2015).
19. M. J. Rooks, C. C. Eugster, J. A. D. Alamo, G. L. Snider, and E. L. Hu, J. Vac. Sci. Technol. B **9**, 2856 (1991).
20. D. R. S. Cumming, S. Thoms, J. M. R. Weaver, and S. P. Beaumont, Microelectron. Eng. **30**, 423 (1996).
21. Y. V. Nastaushev, T. Gavrilova, M. Kachanova, L. Nenasheva, V. Kolosanov, O. V. Naumova, V. P. Popov, and A. L. Aseev, Mater. Sci. Eng. C **19**, 189 (2002).
22. A.-P. Blanchard-Dionne and M. Meunier, J. Vac. Sci. Technol. B **33**, 061602 (2015).
23. R. Andok, A. Bencurova, K. Vutova, E. Koleva, P. Nemec, P. Hrkut, I. Kostic, and G. Mladenov, J. Phys. Conf. Ser. **700**, 012030 (2016).
24. I. Kostic, K. Vutova, R. Andok, V. Barak, A. Bencurova, R. Ritomsky, and T. Tanaka, J. Phys. Conf. Ser. **992**, 012057 (2018).
25. S. Thoms and D. S. Macintyre, J. Vac. Sci. Technol. B **32**, 06FJ01 (2014).